PNAS RESEARCH ARTICLE | CHEMISTRY

In situ generated hydrogen-bonding microenvironment in functionalized MOF nanosheets for enhanced CO_2 electroreduction

Ge Yang[a,1], Jiajia Huang[a,1], Weizhi Gu[b], Zhongyuan Lin[a], Qingyu Wang[c], Rong Kang[a], Jing-Yao Liu[d], Zhihu Sun[c], Xusheng Zheng[c], Long Jiao[b,2], and Hai-Long Jiang[a,2]

Affiliations are included on p. 7.

Edited by C. Jeffrey Brinker, The University of New Mexico, Albuquerque, NM; received September 22, 2024; accepted February 12, 2025

The microenvironment around catalytic sites plays crucial roles in enzymatic catalysis while its precise control in heterogeneous catalysts remains challenging. Herein, the coordinatively unsaturated metal nodes of Hf-based metal-organic framework nanosheets are simultaneously codecorated with catalytically active Co(salen) units and adjacent pyridyl-substituted alkyl carboxylic acids via a post modification route. By varying pyridyl-substituted alkyl carboxylic acids, the spatial positioning of the N atom in pyridine group relative to adjacent Co(salen) can be precisely controlled. Notably, the 3-(pyridin-4-yl)propionic acid, with *para*-position pyridine N atom, maximally improves the electrocatalytic CO_2 reduction performance of Co(salen) unit, far superior to other counterparts. Mechanism investigations reveal that the pyridine unit of 3-(pyridin-4-yl)propionic acid is optimally positioned relative to Co(salen) and undergoes in situ reduction to pyridinyl radical under working potentials. This greatly facilitates the stabilization of *COOH intermediate via hydrogen-bonding interaction, lowering the formation energy barrier of *COOH and therefore boosting CO_2 electroreduction.

metal-organic frameworks | microenvironment | hydrogen bonding | electrocatalysis | CO_2 reduction

Catalytic conversion of waste CO_2 into value-added fuels and chemicals offers significant opportunities for both environmental protection and economic development (1–5). Among different techniques for CO_2 conversion, electrocatalytic CO_2 reduction reaction (CO_2RR) has garnered significant attention for its ability to efficiently convert CO_2 into clean chemical energy under mild conditions (3–9). Unfortunately, due to the higher energy barrier (750 kJ/mol) required to activate C=O bond of CO_2 and the presence of competing H_2 evolution reaction, electrocatalytic CO_2 reduction usually suffers from unsatisfied efficiency and/or selectivity (10–13). To achieve excellent catalytic performance, there remains an urgent need for efficient electrocatalysts.

Inspired by enzyme catalysis, the precise orientation and arrangement of amino acid residues around catalytic sites create unique microenvironment for the elegant catalytic process by reducing the energy barriers through noncovalent interactions (14, 15). For instance, in CO-dehydrogenase (CODH), the histidine in the second coordination sphere can assist the stabilization of key reaction intermediates via hydrogen-bonding interaction, which significantly promotes CO_2 conversion over the Ni–Fe clusters (15). Additionally, the phosphoenolpyruvate carboxykinase and formate dehydrogenase could also stabilize the substrate (such as CO_2 and formate) through hydrogen-bonding interaction, facilitating the efficient progression of catalytic reaction (16, 17). Therefore, in artificial catalysts, the construction of biomimetic microenvironment is a promising way to improve CO_2 electroreduction. Unfortunately, the current research efforts primarily focus on the elaborate design of catalytic sites (8, 11), while the microenvironment surrounding catalytic sites that plays crucial roles in catalysis is largely overlooked. Moreover, there is lack of an effective strategy to atomically precise microenvironment modulation, severely hindering the mechanism understanding and further catalytic performance optimization.

Metal-organic frameworks (MOFs) (18–22), a class of crystalline porous materials constructed by metal ions/clusters and organic linkers, are promising toward diverse applications such as gas adsorption/separation, catalysis, sensing, etc. (23–29) The porous structure of MOFs enables the creation of artificial pockets similar to those in enzymes (30, 31). Besides, thanks to the readily tailorable components and periodic structures, it is feasible for MOFs to integrate diverse functional units and dominate their orientation and arrangement around catalytic sites in a well-controlled manner (32–36). This greatly

Significance

The microenvironment around catalytic sites, created by the precisely arranged amino acid residues, has been proved to play significant roles in enzyme catalysis. Inspired by this, the construction of biomimetic microenvironment is a promising way to improve catalytic performance of artificial catalysts while this remains a great challenge. Our study presents the precise modulation of hydrogen-bonding microenvironment in functionalized metal-organic framework nanosheets by the in situ transformation of pyridinic units under working potentials. The in situ generated hydrogen-bonding microenvironment around catalytically active Co(salen) units facilitates the stabilization of *COOH intermediate and therefore greatly enhances CO_2 electroreduction. This unambiguously demonstrates the significance of microenvironment around catalytic sites and unveils in situ dynamic transformation mechanism during electrocatalysis.

This article is a PNAS Direct Submission.

Copyright © 2025 the Author(s). Published by PNAS. This article is distributed under Creative Commons Attribution-NonCommercial-NoDerivatives License 4.0 (CC BY-NC-ND).

[1]G.Y and J.H. contributed equally to this work.

[2]To whom correspondence may be addressed. Email: longjiao@ustc.edu.cn or jianglab@ustc.edu.cn.

This article contains supporting information online at https://www.pnas.org/lookup/suppl/doi:10.1073/pnas.2419434122/-/DCSupplemental.

Published April 10, 2025.

Downloaded from https://www.pnas.org by UNIVERSITY OF SCIENCE AND TECHNOLOGY OF CHINA on April 10, 2025 from IP address 218.22.21.22.

facilitates the precise control over the microenvironment around catalytic sites to mimic the functions of enzymes for performance optimization (31, 37–40). Moreover, the well-defined MOF structures make them an ideal platform to investigate the structural–performance relationship of microenvironment modulation in catalysis.

With the above in mind, Hf-based MOF nanosheets (MOFNs), with abundant coordinatively unsaturated Hf sites, are employed as the platform for the fabrication of electrocatalysts. Through a straightforward postmodification strategy, the catalytically active Co(salen) units and various pyridyl-substituted alkyl carboxylic acids, namely X-PyC_n (where X is *o*, *m*, or *p* representing the *ortho*-, *meta*-, or *para*-position of pyridine N relative to alkyl chain and n is the carbon atom number of alkyl chains), are attached onto the Hf-oxo clusters, affording Co&X-PyC_n/MOFNs materials (Co represent Co(salen) for short) (Scheme 1). By varying the pyridine N position (*ortho*-, *meta*-, or *para*-) and alkyl chain length of pyridine substituted alkyl carboxylic acids, the corresponding spatial orientation and distance of pyridine N relative to the Co sites in Co&X-PyC_n/MOFNs can be precisely manipulated. As a result, the optimized Co&*p*-PyC_3/MOFNs exhibits significantly improved electrocatalytic performance for CO_2RR with higher CO selectivity at lower overpotentials, superior to other Co&X-PyC_n/MOFNs counterparts with different spatial locations between pyridine N and Co sites as well as Co/MOFNs without pyridine unit. Mechanistic investigations reveal that the pyridine unit in Co&*p*-PyC_3/MOFNs is optimally positioned and undergoes in situ transformation to pyridinyl radical, which facilitates the stabilization of *COOH intermediate through hydrogen-bonding interaction, thereby improving CO_2 electroreduction.

Results and Discussion

A type of representative Hf-based MOFNs, with wrinkled sheet-like morphology, was successfully constructed by the assembly of Hf-oxo clusters and 1,3,5-tri(4-carboxyphenyl)benzene (H_3BTB) linkers (*SI Appendix*, Fig. S1 and S2) (41–43). The excellent stability and tunability of Hf-/Zr-based MOFs make them promising in electrocatalytic applications (44, 45). For MOFNs, there are six coordination sites in the same plane on the 12-connected Hf-oxo cluster to connect BTB linkers, leaving another six unsaturated coordination sites readily to be functionalized by external molecules (*SI Appendix*, Fig. S3) (42). Atomic force microscopy (AFM) observations reveal that Hf-based MOFNs are present as single layers with a thickness of approximately 1.5 nm (*SI Appendix*, Fig. S4), which will benefit the fast electrical electron and mass transfer during catalysis (42). The Co(salen) complex, constructed by incorporating Co ions in the presynthesized salen molecules (*SI Appendix*, Fig. S5 and Table S1), and variable pyridine-substituted alkyl carboxylic acids were then grafted onto the Hf-based MOFNs simultaneously. This was achieved through the coordination of –COOH groups from Co(salen) or pyridine-substituted alkyl carboxylic acids with the coordinatively unsaturated Hf-oxo clusters in the Hf-based MOFNs, resulting in a library of Co&X-PyC_n/MOFNs materials.

The crystallinity, layered morphology, and porous structure of Co&X-PyC_n/MOFNs are all well retained compared with the pristine Hf-based MOFNs (Fig. 1*A* and *SI Appendix*, Figs. S1 and S6–S10). Taking Co&*p*-PyC_3/MOFNs as the representative, the clear lattice fringes and diffraction pattern observed in the high resolution transmission electron microscopy (HRTEM) as well as the corresponding fast Fourier transform (FFT) images further confirm the high crystallinity of MOFNs after post modification (Fig. 1*B* and *SI Appendix*, Fig. S11), in consistence with the powder X-ray diffraction (XRD) analysis (*SI Appendix*, Fig. S1). In addition, Co&*p*-PyC_3/MOFNs presents a thicker layer (~2.9 nm) than pristine Hf-based MOFNs (Fig. 1*C* and *SI Appendix*, Fig. S4), indicating the successful modification of Co(salen) units and pyridine substituted alkyl carboxylic acids. This is further supported by the uniform distribution of Co, N elements over the MOFNs (Fig. 1*D*). As revealed by the diffuse reflectance infrared Fourier transform (DRIFT) spectra, the terminal –OH groups (3,671 cm^{-1}) on the coordinatively unsaturated Hf-oxo clusters in Co&X-PyC_n/MOFNs significantly decreases compared with the pristine MOFNs, suggesting the replacement of –OH after postmodification process (*SI Appendix*, Fig. S12) (46). This confirms the successful coordination of Hf-oxo clusters with –COOH groups in Co(salen) and pyridine substituted alkyl carboxylic acids (39, 46). The ^{1}H nuclear magnetic resonance (NMR) analysis reveals that each Hf-oxo cluster is occupied by one Co(salen) unit and one pyridine substituted alkyl carboxylic acid molecule on average in the Co&X-PyC_n/MOFNs materials (*SI Appendix*,

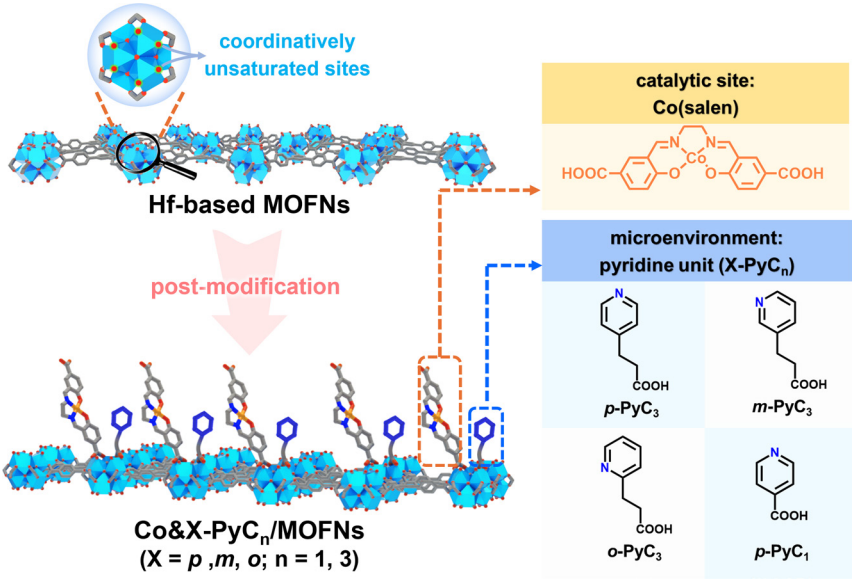

Scheme 1. Schematic illustration for the fabrication and structural analysis of Co&X-PyC_n/MOFNs(X = *p*, *m*, *o*; n = 1, 3).

Downloaded from https://www.pnas.org by UNIVERSITY OF SCIENCE AND TECHNOLOGY OF CHINA on April 10, 2025 from IP address 218.22.21.22.

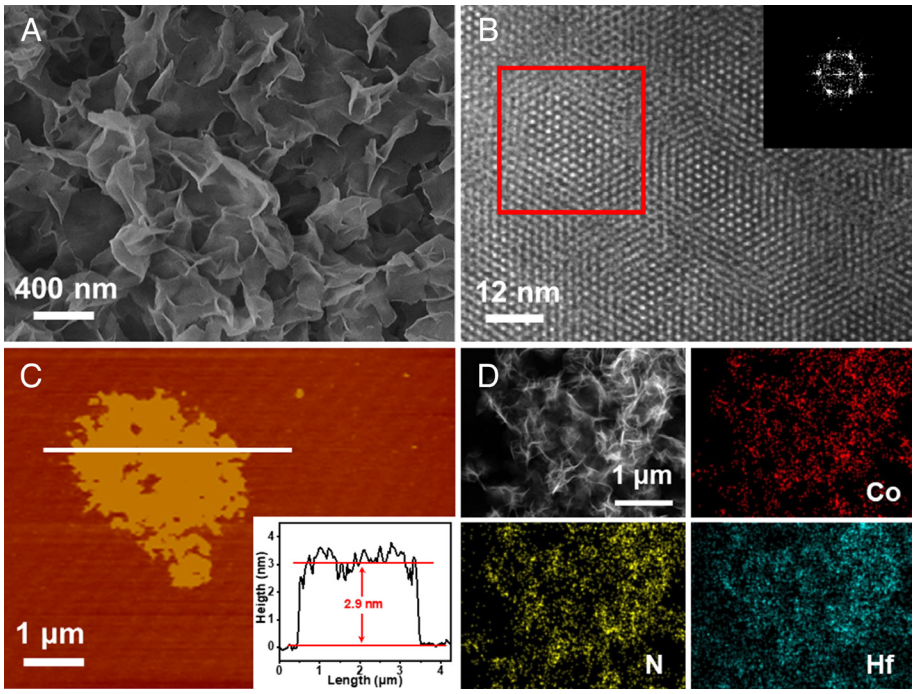

Fig. 1. (*A*) Scanning electron microscopy (SEM), (*B*) HRTEM (*Inset*: the corresponding FFT image of HRTEM), and (*C*) AFM (*Inset*: the height profile) images of Co&*p*-PyC_3/MOFNs. (*D*) The elemental mapping for Co, N, and Hf elements in Co&*p*-PyC_3/MOFNs.

Fig. S13). This arrangement facilitates the close proximity between Co(salen) and pyridine units, enhancing their interaction in subsequent catalysis. Moreover, the contents of Co in various Co&X-PyC_n/MOFNs samples are well controlled at ~1.2 wt%, demonstrating the similar modification amount of Co(salen) in different Co&X-PyC_n/MOFNs materials (*SI Appendix*, Table S2).

The ultraviolet-visible (UV-vis) spectra of Co&X-PyC_n/MOFNs series all display typical absorption peaks of Co(salen) units at 269, 374, and 505 nm (47), identical to Co/MOFNs that is decorated with Co(salen) merely (Fig. 2*A*). This preliminarily excludes the direct chemical interaction (for example, coordination interaction) between Co(salen) and N atom in pyridine substituted alkyl carboxylic acids. Meanwhile, the X-ray photoelectron spectroscopy (XPS) measurements also support the undisturbed electronic states of Co sites (with the valence state of +2) in both Co&X-PyC_n/MOFNs and Co/MOFNs (*SI Appendix*, Fig. S14). Moreover, the unchanged position of L_3 (779.0 and 781.8 eV) and L_2 (796.2 eV) peaks in the Co L-edge near-edge X-ray absorption fine structure (NEXAFS) spectra for these samples further confirms the results of XPS analysis (Fig. 2*B*).

Furthermore, X-ray absorption fine structure (XAFS) spectroscopy has been conducted to provide more information on the existing state of Co sites. The Co K-edge X-ray absorption near-edge structure (XANES) spectra of Co&X-PyC_n/MOFNs as well as Co/MOFNs all locate at higher energy region compared to Co foil and overlap with each other (Fig. 2*C*), suggesting the same oxidation sate of Co. This is in good consistency with XPS and Co L-edge NEXAFS results above (Fig. 2 *B* and *C* and *SI Appendix*, Fig. S14). Moreover, all Co&X-PyC_n/MOFNs and Co/MOFNs present similar Fourier transform-extended X-ray absorption fine structure (FT-EXAFS) spectra with a dominate peak around 1.42 Å originated from Co–N/Co–O bonding (Fig. 2*D*). Further EXAFS fittings confirm the undisturbed primary coordination environment of Co (namely Co-N_2O_2) in all Co&X-PyC_n/MOFNs and Co/MOFNs, which is identical to that in the Co(salen) unit (*SI Appendix*, Figs. S15 and S16 and Table S3). The UV-vis, XPS, NEXAFS, and XAFS results jointly illustrate the undisturbed electronic state and primary coordination environment of Co center in Co(salen) regardless of the existence of proximal pyridine units. This provides an ideal platform to investigate how the pyridine microenvironment influences the catalytic behavior of Co(salen) sites without disturbing their intrinsic properties.

Encouraged by the results above, electrocatalytic CO_2 reduction performance over the above Co-based materials has been examined. The linear sweep voltammetry (LSV) measurements suggest that all Co&X-PyC_n/MOFNs and Co/MOFNs samples present higher current response under CO_2 than those under N_2 atmosphere, demonstrating their potential in electrocatalytic CO_2 reduction (*SI Appendix*, Figs. S17–S21). Specifically, Co&*p*-PyC_3/MOFNs showcase the highest current density under CO_2, underscoring the importance of pyridine units around catalytically active Co(salen) (*SI Appendix*, Fig. S22). Moreover, the CO Faradaic efficiency (FE) of Co&*p*-PyC_3/MOFNs can reach above 90% at −2.5 V vs. Ag/Ag^+ (Fig. 3*A*). In contrast, Co&*m*-PyC_3/MOFNs, Co&*o*-PyC_3/MOFNs, Co&*p*-PyC_1/MOFNs, and Co/MOFNs give the CO FE of 79%, 73%, 66%, and 47% at −2.5 V, much inferior to Co&*p*-PyC_3/MOFNs (Fig. 3*A*). The H_2 is detected as the only byproduct of Co/MOFNs and Co&X-PyC_n/MOFNs materials (*SI Appendix*, Figs. S23 and S24). Meanwhile, Co&*p*-PyC_3/MOFNs exhibit the largest CO partial current density (J_{CO}) under all measured potentials comparing with other catalysts and present excellent stability with well-retained current density and FE of CO (Fig. 3 *B* and *C*). Moreover, the XRD pattern shows the well-retained crystalline structure of Co&*p*-PyC_3/MOFNs after electrocatalysis and no Co leaches into the electrolyte, further confirming the stability of Co&*p*-PyC_3/MOFNs (*SI Appendix*, Fig. S25 and Table S2). In addition, the smallest Tafel slope of Co&*p*-PyC_3/MOFNs indicates its most favorable kinetics among all investigated materials (*SI Appendix*, Fig. S26). For better comparison, *p*-PyC_3/MOFNs and pure MOFNs without Co(salen) modification have also been examined, showing inferior FE of CO and even much lower than Co/MOFNs (*SI Appendix*, Fig. S27). This further confirms that Co(salen) unit is the real catalytic sites and also excludes the activity

Downloaded from https://www.pnas.org by UNIVERSITY OF SCIENCE AND TECHNOLOGY OF CHINA on April 10, 2025 from IP address 218.22.21.22.

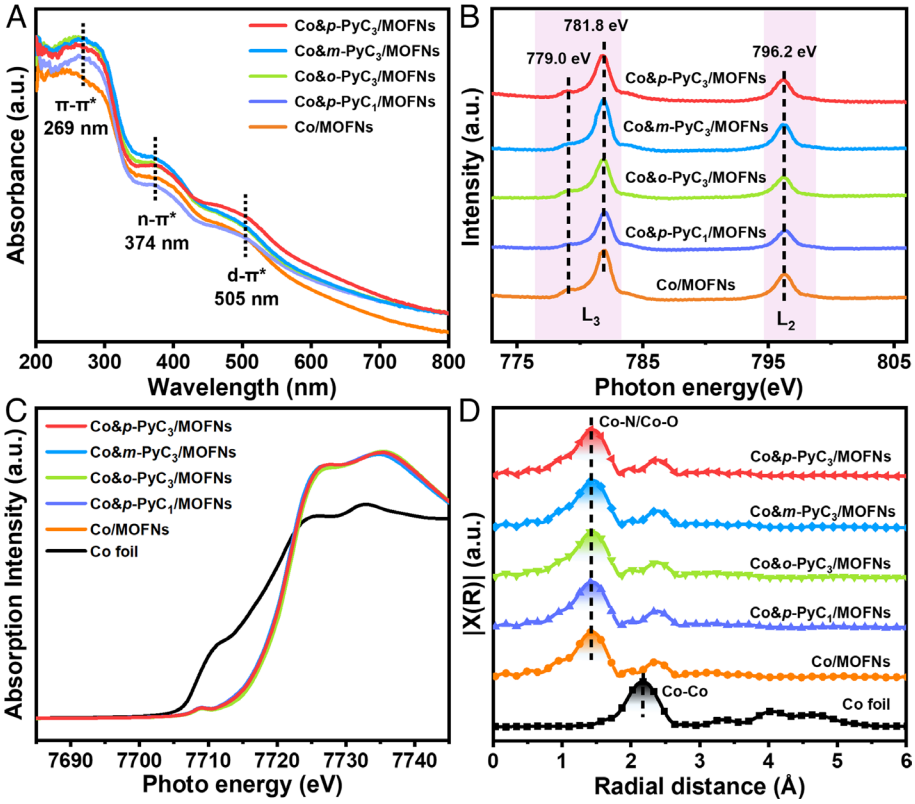

Fig. 2. (*A*) UV-vis spectra, (*B*) Co L-edge NEXAFS spectra, (*C*) Co K-edge XANES spectra, and (*D*) FT-EXAFS spectra of Co&X-PyC$_n$/MOFNs and Co/MOFNs.

of pyridine groups. In addition, the physical mixture of Co/MOFNs and *p*-PyC$_3$/MOFNs exhibits much inferior performance to Co&*p*-PyC$_3$/MOFNs, highlighting the significance of the proximity between Co(salen) and the pyridine groups in Co&*p*-PyC$_3$/MOFNs (*SI Appendix*, Fig. S28). The electrochemical analysis reveals that the pyridine units surrounding the Co(salen) sites, despite not directly interacting with Co(salen) unit, create critical microenvironment that modulates the catalytic performance. Moreover, the performance differences among Co&X-PyC$_n$/MOFNs series suggest that the position of pyridine N relative to Co sites, dominated by altering the types of pyridine-substituted alkyl carboxylic acids, is of great significance (Fig. 3 *A* and *B* and *SI Appendix*, Fig. S26).

To understand the critical role of pyridine units in Co&*p*-PyC$_3$/MOFNs during CO_2 reduction process, more characterizations have been further carried out. Compared with Co/MOFNs, all Co&X-PyC$_n$/MOFNs samples with pyridine units exhibit enhanced CO_2 adsorption capacity, which might be beneficial to the enrichment of CO_2 during electrocatalysis process (*SI Appendix*, Fig. S29). This enhancement can be attributed to the strong interaction between electrophilic carbon atom of CO_2 and the pyridine groups with lone pair of electrons (48). The in situ attenuated total reflectance infrared (ATR-IR) spectra present that the key *COOH intermediate (~1,280 and ~1,350 cm^{-1}) appears at lower overpotential on Co&*p*-PyC$_3$/MOFNs compared to Co/MOFNs (Fig. 4*A*). Moreover, the chemisorbed CO intermediate (*CO: 2,030 cm^{-1}) could also be observed much earlier on Co&*p*-PyC$_3$/MOFNs than Co/MOFNs as the overpotential increases (Fig. 4*B*). The much easier formation of *COOH and *CO in Co&*p*-PyC$_3$/MOFNs reflects that the presence of pyridine units around catalytic Co sites would be able to significantly promote CO_2 conversion.

In addition to the observation of key intermediates during CO_2 electroreduction, the dynamic evolution of Co&*p*-PyC$_3$/MOFNs under applied potentials has also been monitored. As the applied potential increases, the appearance of a broad peak at 3,317 cm^{-1} assigned to the N–H vibration is observed in the in situ ATR-IR spectra of Co&*p*-PyC$_3$/MOFNs, which is absent for Co/MOFNs without pyridine (*SI Appendix*, Figs. S30 and S31). This manifests the possible in situ reduction of pyridine to pyridinyl radical (PyrH$^{\cdot}$) under working potential (49). The cyclic voltammetry (CV) measurements also present the reduction peak at about −2.1 V (vs. Ag/Ag$^+$) for Co&*p*-PyC$_3$/MOFNs, similar to that of methyl 4-pyridinylacetate (4-PyCOOMe) molecules (*SI Appendix*, Figs. S32 *A* and *E* and S33*A*) (50). This manifests the formation of PyrH$^{\cdot}$, which is also proved by the UV-vis spectrum analysis (*SI Appendix*, Fig. S34). In contrast, no reduction peak is observed for Co/MOFNs with poor activity, further confirming the in situ formation of PyrH$^{\cdot}$ in Co&*p*-PyC$_3$/MOFNs under working potentials (*SI Appendix*, Fig. S33*B*). Moreover, as revealed by in situ ATR-IR and CV analysis, the potential for the emergence of PyrH$^{\cdot}$ in Co&*p*-PyC$_3$/MOFNs coincides with that of *COOH formation (Fig. 4*B* and *SI Appendix*, Figs. S30 and S32*A*). This reveals that the PyrH$^{\cdot}$ species generated in situ would create particular microenvironment around Co(salen) to accelerate the *COOH formation during CO_2 electroreduction. Although similar reduction peaks of PyrH$^{\cdot}$ are also observed for the other Co&X-PyC$_n$/MOFNs, their performance in CO_2 electroreduction is inferior to that of Co&*p*-PyC$_3$/MOFNs (Fig. 3*A* and *SI Appendix*, Fig. S32 *B–D*), which might be due to the differences of the spatial position and distance of pyridine N relative to Co(salen).

Theoretical calculations have been employed to further investigate the specific roles of in situ generated PyrH$^{\cdot}$ radical. Initially, the direct interaction between *COOH intermediate and PyrH$^{\cdot}$ species is attempted, while it fails due to the relatively long distance between *COOH and PyrH$^{\cdot}$ species (*SI Appendix*, Fig. S35). This inspires us to take into account the role of the electrolyte. The trifluoroethanol (TFE) in the electrolyte, a polar molecule which could potentially interact with *COOH intermediate and PyrH$^{\cdot}$ species, may play roles in the CO_2 electroreduction. Delightfully, via configuration optimization, it is found that the –OH group of TFE would be able

Downloaded from https://www.pnas.org by UNIVERSITY OF SCIENCE AND TECHNOLOGY OF CHINA on April 10, 2025 from IP address 218.22.21.22.

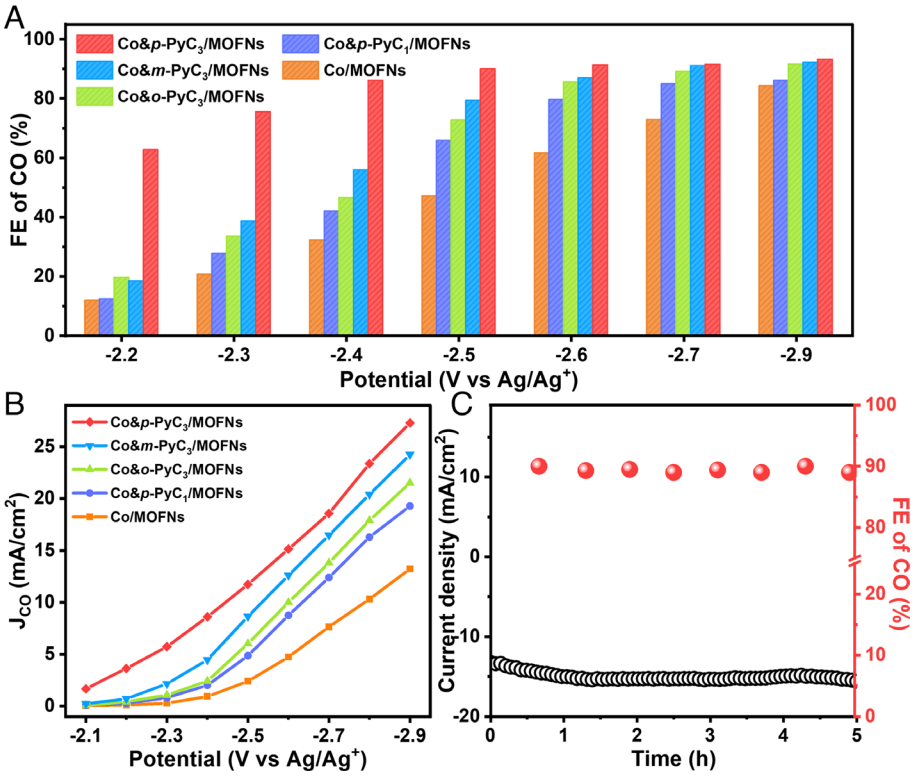

Fig. 3. (*A*) FEs of CO and (*B*) CO partial current densities of Co&X-PyC$_n$/MOFNs and Co/MOFNs in CO_2-saturated electrolyte. (*C*) The stability test of Co&*p*-PyC$_3$/MOFNs for CO_2 electroreduction at −2.5 V.

to perfectly bridge the distance gap between *COOH and PyrH$^{\cdot}$, forming *COOH···TFE···PyrH$^{\cdot}$ triad state via hydrogen-bonding interaction (Fig. 5*A* and *SI Appendix*, Fig. S36). Besides, DFT calculations also exclude the possibility of hydrogen bonding between the –OH group of TFE and the N atom of Co(salen), ruling out the interaction between Co(salen) and TFE (*SI Appendix*, Fig. S37). To experimentally verify the formation *COOH···TFE···PyrH$^{\cdot}$ triad species via H-bonding interaction, ^{1}H NMR spectroscopy is adopted. Since PyrH$^{\cdot}$ and *COOH species are in situ formed during reaction and are difficult to isolate out, pyrrole (with similar N–H unit to PyrH$^{\cdot}$) is employed to simulate PyrH$^{\cdot}$, and 2-chloro-2,2-difluoroacetic acid (with similar pK_a to the *COOH intermediate) is employed as the simulant for *COOH (*SI Appendix*, Fig. S38 and Table S4). Obvious concentration-dependent peak shifts are observed for TFE with different concentrations of 2-chloro-2,2-difluoroacetic acid, indicating the significant hydrogen-bonding interaction between *COOH and TFE (Fig. 5*B*) (51, 52). Moreover, similar peak shifts are also observed for pyrrole with different concentrations of TFE due to the formation of TFE···PyrH$^{\cdot}$ interaction (Fig. 5*C*). By adding different amounts of trifluorotoluene (TFT) which contains similar –CF_3 group to TFE but lacks the –OH group in the pyrrole solution, the characteristic peak of the active hydrogen in pyrrole shows negligible chemical shift (*SI Appendix*, Fig. S39). This suggests the absence of F···H hydrogen bonds between PyrH$^{\cdot}$ and –CF_3 group of TFE, which is further supported by theoretical calculations (*SI Appendix*, Fig. S40). The NMR results clearly support the formation of *COOH···TFE···PyrH$^{\cdot}$ via hydrogen-bonding interaction bridged by the –OH group of TFE, further unveiling the mechanism behind the easier formation of *COOH in Co&*p*-PyC$_3$/MOFNs than that in Co/MOFNs (Fig. 5*A* and *SI Appendix*, Figs. S36 and S41). Consequently, the Gibbs free energy difference (ΔG) for *COOH formation in this case is

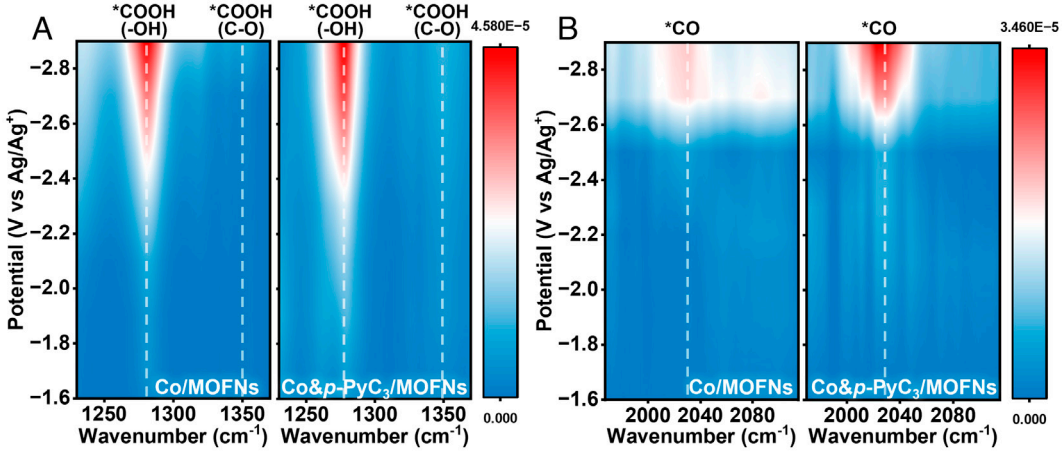

Fig. 4. In situ ATR-IR spectra of Co/MOFNs and Co&*p*-PyC$_3$/MOFNs for (*A*) *COOH and (*B*) *CO species under different applied potentials.

Downloaded from https://www.pnas.org by UNIVERSITY OF SCIENCE AND TECHNOLOGY OF CHINA on April 10, 2025 from IP address 218.22.21.22.

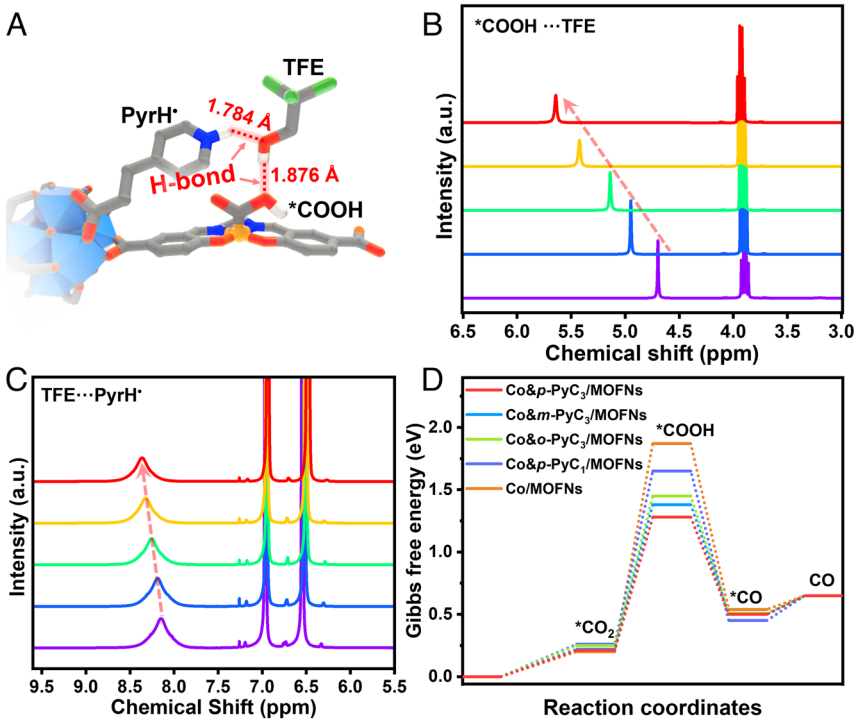

Fig. 5. (*A*) The illustration of *COOH···TFE···PyrH· state formed via hydrogen-bonding interaction. (*B*) The ^{1}H NMR spectra of trifluoroethanol with different concentrations of 2-chloro-2,2-difluoroacetic acid. (*C*) The ^{1}H NMR spectra of pyrrole with different concentrations of trifluoroethanol. (*D*) Gibbs free energy diagram of different catalysts during electrochemical CO_2 reduction.

determined to be 1.07 eV over Co&*p*-PyC$_3$/MOFNs, much smaller than that over Co/MOFNs (1.67 eV) (Fig. 5*D* and *SI Appendix*, Fig. S42).

In addition to Co&*p*-PyC$_3$/MOFNs, other kinds of pyridine microenvironment in Co&X-PyC$_n$/MOFNs materials have been also investigated. It is found that all Co&*p*-PyC$_1$/MOFNs, Co&*o*-PyC$_3$/MOFNs, and Co&*m*-PyC$_3$/MOFNs showcase much larger ΔG(*COOH) than Co&*p*-PyC$_3$/MOFNs (Fig. 5*D* and *SI Appendix*, Figs. S43–S46). This further implies that the pyridine N atom in Co&*p*-PyC$_3$/MOFNs occupies the optimal spatial location (relative distance and spatial orientation) relative to Co(salen) unit, favorable to the stabilization of *COOH via hydrogen-bonding interaction and improving the electrocatalytic CO_2 reduction process (Fig. 5*D* and *SI Appendix*, Figs. S42–S46).

Conclusions

In summary, a series of Co&X-PyC$_n$/MOFNs materials, involving Co(salen) as catalytic sites and proximal pyridine as the microenvironment, are fabricated via a facile postmodification strategy. The variation of the decorated pyridyl-substituted alkyl carboxylic acids achieves the precise regulation over the spatial distance and orientation of pyridine groups relative to Co(salen) at atomic scale. Among these samples, the optimized Co&*p*-PyC$_3$/MOFNs, with *para*-pyridine N and most appropriate alkyl chain length, exhibits far superior FE of CO to other Co&X-PyC$_n$/MOFNs counterparts as well as Co/MOFNs without pyridine units. Experimental investigations combined with computational analysis demonstrate that pyridine units around Co(salen) are dynamically converted to reduced pyridinyl radical (PyrH·) during electrocatalysis, which can collaborate with TFE molecule in electrolyte. Given the optimal spatial compatibility between pyridine and Co(salen) unit, Co&*p*-PyC$_3$/MOFNs can form stable *COOH···TFE···PyrH· triad species via hydrogen-bonding interaction, greatly stabilizing the *COOH intermediate and minimizing reaction energy barrier. This work offers a straightforward strategy for precise microenvironment modulation around catalytic sites and unveils the in situ transformation mechanism of microenvironment units for enhanced catalytic performance.

Materials and Methods

Synthesis of Salendicarboxylic Acid. The synthesis of salendicarboxylic acid (named salen for short) followed the procedures reported previously (53). Typically, 3-formyl-4-hydroxybenzoic acid (1.08 g, 6.5 mmol) was completely dissolved in ethanol (30 mL). A solution of ethylenediamine (217 μL, 3.25 mmol) in ethanol (30 mL) was added dropwise to the above solution at room temperature with continuous stirring. The mixture was heated at 90 °C by refluxing overnight. After cooling down to room temperature, the yellow powder was obtained by filtration, washed with ethanol, and dried at 85 °C overnight.

Synthesis of Co-Salendicarboxylic Acid Complex. The Co-salendicarboxylic acid complex (named as Co(salen) for short) was prepared according to the previous report with some modifications (53). Typically, salen (340 mg, 0.72 mmol) was dissolved in DMF (80 mL) under a nitrogen atmosphere. A solution of $Co(OAc)_2{\cdot}4H_2O$ (168 mg, 0.84 mmol) in DMF (20 mL) was added dropwise to the DMF solution of salen. After stirring at room temperature for 3 h, most DMF was removed from the above mixture by rotary evaporation. After that, H_2O (200 mL) was added, and the precipitate was obtained by filtration, washed with H_2O, and dried at 85 °C overnight.

Synthesis of Hf-Based MOFNs. The Hf-based MOFNs was synthesized according to the previous report with some modification (54). Typically, $HfCl_4$ (14 mg) and 1,3,5-tri(4-carboxyphenyl) benzene (H_3BTB, 12.5 mg) were dissolved in DMF (3 mL) in pyrex vials. After that, H_2O (150 μL) and HCOOH (750 μL) were added to the solution above. The mixture was kept at 120 °C for 48 h in the oven. After cooling down to room temperature, the white precipitate was obtained by centrifugation and washing with DMF several times.

Synthesis of Co/MOFNs and Co&X-PyC$_n$/MOFNs. Taking Co&*p*-PyC$_3$/MOFNs as an example, the obtained Hf-based MOFNs were dispersed in DMF solution (5 mL) containing 4-pyridine propionic acid (*p*-PyC$_3$) (0.13 mmol). The Co(salen) complex (0.05 mmol) was then added to the above solution and the resulting mixture was heated at 80 °C for 12 h. After cooling down to room temperature, the brown powder was obtained by centrifugation and washed with DMF several times to remove

Downloaded from https://www.pnas.org by UNIVERSITY OF SCIENCE AND TECHNOLOGY OF CHINA on April 10, 2025 from IP address 218.22.21.22.

the unreacted modifiers. Finally, the powder of Co&*p*-PyC_3/MOFNs was acquired by freeze-drying. The Co&*o*-PyC_3/MOFNs, Co&*m*-PyC_3/MOFNs, and Co&*p*-PyC_1/MOFNs were synthesized following the same procedure as Co&*p*-PyC_3/MOFNs with the addition of 2-pyridine propionic acid (*o*-PyC_3), 3-pyridine propionic acid (*m*-PyC_3), and 4-pyridine carboxylic acid (*p*-PyC_1), respectively, instead of *p*-PyC_3. The Co/MOFNs can be synthesized following the same procedure as Co&*p*-PyC_3/MOFNs without the addition of *p*-PyC_3.

Instruments. Detailed information for instruments has been provided in *SI Appendix*, *Text S1*.

Electrochemical Measurements. Detailed information for electrochemical measurements has been provided in *SI Appendix*, *Text S2*.

Computational Details. Detailed information for theoretical computations has been provided in *SI Appendix*, *Text S3*.

Data, Materials, and Software Availability. All study data are included in the article and/or *SI Appendix*.

ACKNOWLEDGMENTS. This work was supported by the National Key Research and Development Program of China (2021YFA1500402), National Natural Science Foundation of China (22331009, U22A20401, 22222507, and 22375193), the Strategic Priority Research Program of the Chinese Academy of Sciences (XDB0450302, XDB0540000), Major Industrial Innovation Plan of Anhui Province (AHZDCYCX-LSDT2023-04), and Postdoctoral Fellowship Program of China Postdoctoral Science Foundation (GZC20232532). We thank the beamline 1W1B station at the Beijing Synchrotron Radiation Facility and the beamline BL10B station at the National Synchrotron Radiation Laboratory in Hefei for synchrotron radiation measurements. The calculations in this work are supported by the Supercomputing Center of University of Science and Technology of China (USTC) and Hefei Advanced Computing Center for providing computational resources. This work was partially carried out at the Instruments Center for Physical Science, USTC.

Author affiliations: [a]Hefei National Research Center for Physical Sciences at the Microscale, Department of Chemistry, University of Science and Technology of China, Hefei, Anhui 230026, People's Republic of China; [b]Key Laboratory of Precision and Intelligent Chemistry, University of Science and Technology of China, Hefei, Anhui 230026, People's Republic of China; [c]National Synchrotron Radiation Laboratory, University of Science and Technology of China, Hefei, Anhui 230029, People's Republic of China; and [d]Laboratory of Theoretical and Computational Chemistry, Institute of Theoretical Chemistry, College of Chemistry, Jilin University, Changchun, Jilin 130023, People's Republic of China

Author contributions: L.J. and H.-L.J. conceived the idea; L.J. and H.-L.J. led the project; G.Y. designed the experiments; G.Y. performed the experiments; J.H. and J.-Y.L. performed the theoretical calculations; G.Y., W.G., Z.L., R.K., L.J., and H.-L.J. analyzed the data; Q.W. and X.Z. supported the soft X-ray measurements; Q.W., X.Z., and Z.S. helped with the X-ray absorption fine structure analysis; and G.Y., L.J., and H.-L.J. co-wrote the manuscript.

The authors declare no competing interest.

1. A. Álvarez *et al.*, Challenges in the greener production of formates/formic acid, methanol, and DME by heterogeneously catalyzed CO_2 hydrogenation processes. *Chem. Rev.* **117**, 9804–9838 (2017).
2. L.-L. Ling *et al.*, Promoted hydrogenation of CO_2 to methanol over single-atom Cu sites with Na^+-decorated microenvironment. *Natl. Sci. Rev.* **11**, nwae114 (2024).
3. B. Chang *et al.*, Electrochemical reduction of carbon dioxide to multicarbon (C_{2+}) products: Challenges and perspectives. *Energy Environ. Sci.* **16**, 4714–4758 (2023).
4. S. Mukhopadhyay *et al.*, Local CO_2 reservoir layer promotes rapid and selective electrochemical CO_2 reduction. *Nat. Commun.* **15**, 3397 (2024).
5. P. Wei *et al.*, Coverage-driven selectivity switch from ethylene to acetate in high-rate CO_2/CO electrolysis. *Nat. Nanotechnol.* **18**, 299–306 (2023).
6. X. Chen *et al.*, Highly stable layered coordination polymer electrocatalyst toward efficient CO_2-to-CH_4 conversion. *Adv. Mater.* **36**, 2310273 (2024).
7. A. Wagner, C. D. Sahm, E. Reisner, Towards molecular understanding of local chemical environment effects in electro- and photocatalytic CO_2 reduction. *Nat. Catal.* **3**, 775–786 (2020).
8. W. Zhang *et al.*, Exclusive Co-N_4 sites confined in two-dimensional metal-organic layers enabling highly selective CO_2 electroreduction at industrial-level current. *Angew. Chem. Int. Ed.* **62**, e202219241 (2023).
9. H.-L. Zhu *et al.*, Continuously producing highly concentrated and pure acetic acid aqueous solution via direct electroreduction of CO_2. *J. Am. Chem. Soc.* **146**, 1144–1152 (2024).
10. M. Zheng *et al.*, Electrocatalytic CO_2-to-C_{2+} with ampere-level current on heteroatom-engineered copper via tuning *CO intermediate coverage. *J. Am. Chem. Soc.* **144**, 14936–14944 (2022).
11. P.-C. Chen *et al.*, Chemical and structural evolution of AgCu catalysts in electrochemical CO_2 reduction. *J. Am. Chem. Soc.* **145**, 10116–10125 (2023).
12. Q. Zhang *et al.*, Coupling of electrocatalytic CO_2 reduction and CH_4 oxidation for efficient methyl formate electrosynthesis. *Energy Environ. Sci.* **17**, 2309–2314 (2024).
13. S. Jin, Z. Hao, K. Zhang, Z. Yan, J. Chen, Advances and challenges for the electrochemical reduction of CO_2 to CO: From fundamentals to industrialization. *Angew. Chem. Int. Ed.* **60**, 20627–20648 (2021).
14. C. Van Stappen *et al.*, Designing artificial metalloenzymes by tuning of the environment beyond the primary coordination sphere. *Chem. Rev.* **122**, 11974–12045 (2022).
15. S. T. Stripp *et al.*, Second and outer coordination sphere effects in nitrogenase, hydrogenase, formate dehydrogenase, and CO dehydrogenase. *Chem. Rev.* **122**, 11900–11973 (2022).
16. J. J. Cotelesage *et al.*, How does an enzyme recognize CO_2? *Int. J. Biochem. Cell B* **39**, 1204–1210 (2007).
17. J. C. Boyington, V. N. Gladyshev, S. V. Khangulov, T. C. Stadtman, P. D. Sun, Crystal structure of formate dehydrogenase H: Catalysis involving Mo, molybdopterin, selenocysteine, and an Fe_4S_4 cluster. *Science* **275**, 1305–1308 (1997).
18. H. C. Zhou, J. R. Long, O. M. Yaghi, Introduction to metal–organic frameworks. *Chem. Rev.* **112**, 673–674 (2012).
19. H. Furukawa, K. E. Cordova, M. O'Keeffe, O. M. Yaghi, The chemistry and applications of metal-organic frameworks. *Science* **341**, 1230444 (2013).
20. T. Islamoglu *et al.*, Postsynthetic tuning of metal-organic frameworks for targeted applications. *Acc. Chem. Res.* **50**, 805–813 (2017).
21. X. Zhao, Y. Wang, D. S. Li, X. Bu, P. Feng, Metal-organic frameworks for separation. *Adv. Mater.* **30**, e1705189 (2018).
22. H. Li *et al.*, Porous metal-organic frameworks for gas storage and separation: Status and challenges. *EnergyChem* **1**, 100006 (2019).
23. W. Wang, D. Chen, F. Li, X. Xiao, Q. Xu, Metal-organic-framework-based materials as platforms for energy applications. *Chem* **10**, 86–133 (2024).
24. L. Jiao, Y. Wang, H.-L. Jiang, Q. Xu, Metal-organic frameworks as platforms for catalytic applications. *Adv. Mater.* **30**, e1703663 (2018).
25. R. Sakamoto *et al.*, Layered metal–organic frameworks and metal–organic nanosheets as functional materials. *Coord. Chem. Rev.* **472**, 214787 (2022).
26. L. Jiao, J. Y. R. Seow, W. S. Skinner, Z. U. Wang, H.-L. Jiang, Metal-organic frameworks: Structures and functional applications. *Mater. Today* **27**, 43–68 (2019).
27. J. Guo *et al.*, Metal-organic frameworks as catalytic selectivity regulators for organic transformations. *Chem. Soc. Rev.* **50**, 5366–5396 (2021).
28. H. Wang *et al.*, Regulating interaction with surface ligands on Au_{25} nanoclusters by multivariate metal-organic framework hosts for boosting catalysis. *Natl. Sci. Rev.* **11**, nwae252 (2024).
29. X.-D. Zhang, S.-Z. Hou, J.-X. Wu, Z.-Y. Gu, Two-dimensional metal-organic framework nanosheets with cobalt-porphyrins for high-performance CO_2 electroreduction. *Chem. Eur. J.* **26**, 1604–1611 (2020).
30. W. Xu *et al.*, Atomic-level design of metalloenzyme-like active pockets in metal-organic frameworks for bioinspired catalysis. *Chem. Soc. Rev.* **53**, 137–162 (2024).
31. L. Jiao, J. Wang, H.-L. Jiang, Microenvironment modulation in metal-organic framework-based catalysis. *Acc. Mater. Res.* **2**, 327–339 (2021).
32. Z.-H. Zhu *et al.*, A facile strategy to obtain low-cost and high-performance gold-based catalysts from artificial electronic waste by $[Zr_{48}Ni_6]$ nano-cages in MOFs for CO_2 electroreduction to CO. *Angew. Chem. Int. Ed.* **61**, e202214243 (2022).
33. G. Lan *et al.*, Biomimetic active sites on monolayered metal–organic frameworks for artificial photosynthesis. *Nat. Catal.* **5**, 1006–1018 (2022).
34. J. Wei *et al.*, Metal-organic capsules with NADH mimics as switchable selectivity regulators for photocatalytic transfer hydrogenation. *J. Am. Chem. Soc.* **141**, 12707–12716 (2019).
35. S. Wang *et al.*, Linker engineering of sandwich-structured metal–organic framework composites for optimized photocatalytic H_2 production. *Adv. Mater.* **35**, e2302512 (2023).
36. J. Pang *et al.*, Precisely embedding active sites into a mesoporous Zr-framework through linker installation for high-efficiency photocatalysis. *J. Am. Chem. Soc.* **142**, 15020–15026 (2020).
37. Y. Zhang *et al.*, Coordination environment dependent selectivity of single-site-Cu enriched crystalline porous catalysts in CO_2 reduction to CH_4. *Nat. Commun.* **12**, 6390 (2021).
38. D.-H. Nam *et al.*, Intermediate binding control using metal-organic frameworks enhances electrochemical CO_2 reduction. *J. Am. Chem. Soc.* **142**, 21513–21521 (2020).
39. G. Yang *et al.*, Turning on asymmetric catalysis of achiral metal-organic frameworks by imparting chiral microenvironment. *Angew. Chem. Int. Ed.* **62**, e202308089 (2023).
40. T. C. Zhuo *et al.*, H-bond-mediated selectivity control of formate versus CO during CO_2 photoreduction with two cooperative Cu/X sites. *J. Am. Chem. Soc.* **143**, 6114–6122 (2021).
41. R. Wang *et al.*, Porous zirconium metal-organic framework constructed from 2D → 3D interpenetration based on a 3,6-connected kgd net. *Inorg. Chem.* **53**, 7086–7088 (2014).
42. W. Shi *et al.*, Surface modification of two-dimensional metal-organic layers creates biomimetic catalytic microenvironments for selective oxidation. *Angew. Chem. Int. Ed.* **56**, 9704–9709 (2017).
43. J. Ma, A. G. Wong-Foy, A. J. Matzger, The role of modulators in controlling layer spacings in a tritopic linker based zirconium 2D microporous coordination polymer. *Inorg. Chem.* **54**, 4591–4593 (2015).
44. S. Yuan *et al.*, Stable metal-organic frameworks: Design, synthesis, and applications. *Adv. Mater.* **30**, 1704303 (2018).
45. J. Zhang *et al.*, Neighboring Zn–Zr sites in a metal-organic framework for CO_2 hydrogenation. *J. Am. Chem. Soc.* **143**, 8829–8837 (2021).
46. P. Deria *et al.*, Perfluoroalkane functionalization of NU-1000 via solvent-assisted ligand incorporation: Synthesis and CO_2 adsorption studies. *J. Am. Chem. Soc.* **135**, 16801–16804 (2013).
47. X. Kong *et al.*, Co-based molecular catalysts for efficient CO_2 reduction via regulating spin states. *Appl. Catal., B* **290**, 120067 (2021).
48. X. Luo *et al.*, Significant improvements in CO_2 capture by pyridine-containing anion-functionalized ionic liquids through multiple-site cooperative interactions. *Angew. Chem. Int. Ed.* **53**, 7053–7057 (2014).
49. H. J. Jang *et al.*, Polypyrrole film synthesis via solution plasma polymerization of liquid pyrrole. *Appl. Surf. Sci.* **608**, 155129 (2023).
50. E. Lebègue, J. Agullo, M. Morin, D. Bélanger, The role of surface hydrogen atoms in the electrochemical reduction of pyridine and CO_2 in aqueous electrolyte. *ChemElectroChem* **1**, 1013–1017 (2014).
51. Y. Luo *et al.*, Binding energy as driving force for controllable reconstruction of hydrogen bonds with molecular scissors. *J. Am. Chem. Soc.* **142**, 6085–6092 (2020).
52. S. Shi *et al.*, Selective hydrogenation via precise hydrogen bond interactions on catalytic scaffolds. *Nat. Commun.* **14**, 429 (2023).
53. S. Eyele-Mezui, E. Delahaye, G. Rogez, P. Rabu, Functional hybrid materials based on layered simple hydroxide hosts and dicarboxylate schiff base metal complex guests. *Eur. J. Inorg. Chem.* **2012**, 5225–5238 (2012).
54. Y. Guo *et al.*, Cooperative stabilization of the [pyridinium-CO_2-Co] adduct on a metal-organic layer enhances electrocatalytic CO_2 reduction. *J. Am. Chem. Soc.* **141**, 17875–17883 (2019).

Downloaded from https://www.pnas.org by UNIVERSITY OF SCIENCE AND TECHNOLOGY OF CHINA on April 10, 2025 from IP address 218.22.21.22.